Chapter 8

Au Nanoparticle Synthesis Via Femtosecond Laser-Induced Photochemical Reduction of $[AuCl_4]^-$

Mallory G. John, Victoria Kathryn Meader and Katharine Moore Tibbetts

Additional information is available at the end of the chapter

http://dx.doi.org/10.5772/intechopen.75075

Abstract

Laser-assisted metallic nanoparticle synthesis is a versatile "green" method that has become a topic of active research. This chapter discusses the photochemical reaction mechanisms driving $[AuCl_4]^-$ reduction using femtosecond-laser irradiation, and reviews recent advances in Au nanoparticle size-control. We begin by describing the physical processes underlying the interactions between laser pulses and the condensed media, including optical breakdown and supercontinuum emission. These processes produce a highly reactive plasma containing free electrons, which reduce $[AuCl_4]^-$, and radical species producing H_2O_2 that cause autocatalytic growth of Au nanoparticles. Then, we discuss the reduction kinetics of $[AuCl_4]^-$, which follow an autocatalytic rate law in which the first- and second-order rate constants depend on free electrons and H_2O_2 availability. Finally, we explain strategies to control the size of gold nanoparticles as they are synthesized; including modifications of laser parameters and solution compositions.

Keywords: femtosecond laser pulses, nanocolloids, optical breakdown, gold nanoparticles, in-situ spectroscopy, photochemical reduction mechanisms

1. Introduction

The unique chemical and physical qualities of metallic nanoparticles have attracted the attention of researchers. Their size- and shape-dependent optical properties make them especially appealing due to the potential technological applications [1–4]. In particular, gold nanoparticles (AuNPs) have strong absorptions in the visible spectrum that come from the collective oscillations of surface conduction-band electrons as they interact with light, which is called the surface plasmon resonance (SPR). The dependence of the SPR absorption on particle size and shape

opens a range of application possibilities for AuNPs, including surface enhanced Raman spectroscopy [5]; non-invasive diagnostic imaging [2]; photothermal cancer therapy [3, 6]; plasmon-enabled photochemistry; and catalytic reactions such as water-splitting [7, 8]. It is necessary to these ends that the NP sizes and shapes are controllable during synthesis [9, 10]. Control can be achieved chemically, by modifying experimental conditions like temperature, reaction time, metal-ion concentration, and the absence or presence of reducing agents and surfactants [2]. Laser-assisted approaches to AuNP fabrication allow the manufacture of "pure" NPs which lack chemical reducing agents or surfactants, making this synthesis method ideal for NPs intended to be used in catalysis, and other electronic, biological or medical applications [11, 12].

There are two common approaches to colloidal AuNP synthesis using laser-assisted methods. The first is bulk-metal ablation, in which metal atoms are ejected from the target material and form nanoparticles in solution [13]. The second is by irradiating a metal-salt solution to produce reducing agents via solvent-molecule photolysis [14–16]. Controlling nucleation and growth of the nanoparticles during metal-salt reduction by changing laser parameters (focusing conditions, pulse duration, pulse energy, irradiation time), and chemical parameters (metal-ion concentration, solvent composition, presence of capping agents), determines the size, shape, and stability of the colloidal products [14–30]. Laser-assisted AuNP fabrication requires a simple setup, which facilitates experimentation [12].

Section 2 of this chapter examines $[AuCl_4]^-$ reduction under femtosecond-laser irradiation, specifically the microplasma formation that arises from optical breakdown (OB) and super continuum emission (SCE). We review both theoretical models for OB and SCE, and provide experimental measurements of both OB and SCE to show which dominates each set of experimental conditions. In Section 3, we describe the chemical reactions that cause photochemical $[AuCl_4]^-$ reduction and AuNP formation, and compare them with the observed autocatalytic reduction kinetics. We relate observed first- and second-order autocatalytic rate constants to the availability of reducing species in the microplasma. Lastly, in Section 4, we review recent literature that describes control over AuNP size- and shape-control through manipulation of laser conditions and chemical composition of the solution.

2. Background: interactions of ultrashort laser pulses with condensed media

In a dielectric medium with a band gap that exceeds the laser photon-energy, ultrashort laser pulses can produce quasi-free electrons in the conduction band by two processes: (1) nonlinear multiphoton ionization and tunneling photoionization [31], and (2) high-kinetic-energy free electron collisions with neutral molecules, causing cascade ionization, also called avalanche ionization [32]. The formation of free electrons initially generates a localized, weakly-ionized plasma [32–34], which can initiate optical breakdown (OB), supercontinuum emission (SCE), or both [35–37]. This section provides an overview of the theory behind both processes, and some experimental measurements.

http://dx.doi.org/10.5772/intechopen.75075

2.1. Optical breakdown

Optical breakdown (OB) of a transparent dielectric medium occurs when the free-electron density ρ_e in plasma exceeds a critical value, and depends on the peak intensity I of the excitation pulse [32–34]. Recent experiments in water have quantified the critical value for ρ_e as the threshold for cavitation-bubble formation at $\rho_e = 1.8 \times 10^{20}$ cm^{-3} [38]. In order to calculate the electron density resulting from the laser–medium interaction, media such as water and other solvents are typically modeled as a dielectric, with band gap Δ. For water, the band gap is usually specified as $\Delta = 6.5$ eV [33, 34], although some recent experiments have placed the effective band gap as high as 9.5 eV for direct excitation into the conduction band [39, 40].

Conventionally, the laser pulse propagates in the z direction with a time-dependent Gaussian intensity envelope based on the focusing conditions [41],

$$I(z,t) = \frac{P(t,z)}{A(z)} = \frac{E_p}{\tau_p \pi w(z)^2} \exp\left[(-4\ln 2)\left(\frac{t - z/c}{\tau_p}\right)^2\right]; \quad w(z) = w_0\sqrt{1 + \frac{z^2}{z_R^2}} \tag{1}$$

where $P(t,z)$ is the time-dependent power density, $A(z)$ the cross-sectional area, E_p the pulse energy, τ_p the pulse duration, c the speed of light, w_0 the beam waist at the focus, and z_R the Rayleigh range.

The time evolution of the free-electron density ρ_e produced by the laser–water interaction is governed by the differential equation [33]

$$\frac{\partial \rho_e}{\partial t} = W_{\text{photo}} + W_{\text{casc}}\rho_e - W_{\text{diff}}\rho_e - W_{\text{rec}}\rho_e^2. \tag{2}$$

Free electrons are produced according to the photoionization rate W_{photo} and cascade ionization rate W_{casc}, while electrons are lost from the focal volume at diffusion rate W_{diff}, and recombination rate W_{rec}. The specific formulas describing each rate are reviewed elsewhere [33, 34].

At a given laser wavelength, the peak-intensity needed to reach critical electron density for OB is highly dependent on pulse duration, due to the interplay between the photoionization and cascade ionization rates [33, 34]. To illustrate this effect over a wide range of pulse durations used in recent $[AuCl_4]^-$ photochemical reduction studies [14–30], Eq.(2) coupled to the appropriate formulas for each rate [33, 34] was solved using the Runge–Kutta integrator `ode45` incorporated into MATLAB, as in our previous work [16]. The critical electron density threshold was taken to be the recently reported experimental value $\rho_e = 1.8 \times 10^{20}$ cm^{-3} [38]. **Figure 1(a)** shows the calculated time-dependent electron density $\rho_e(t)$ for pulses at intensity $I = 10^{13}$ W cm^{-2} with durations of 30 fs (dark blue), 100 fs (light blue), 200 fs (green), 1.5 ps (orange), and 36 ps (red). The value of zero on the abscissa corresponds to the center of the pulse, and the time is normalized to the respective pulse durations. The dashed line at $\rho_e = 1.8 \times 10^{20}$ cm^{-3} indicates the OB threshold. The rise in peak electron density with pulse duration results from the increased

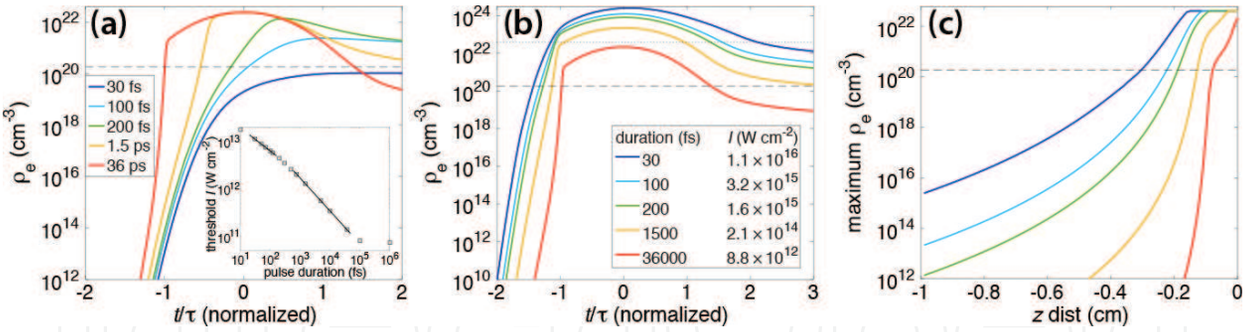

Figure 1. (a) Electron density vs. time for 1×10^{13} W cm^{-2} pulses with a series of durations from 30 fs to 36 ps. Inset: Threshold intensity required to achieve OB as a function of pulse duration. (b) Electron density vs. time for 1 mJ pulses. (c) Electron density vs. propagation distance z from the geometric focus for 1 mJ pulses.

contribution of cascade ionization to the formation of free electrons as the pulse lengthens [33, 34]. As a result, the threshold intensity to achieve OB decreases by two orders of magnitude as the pulse duration is increased from 30 fs to 36 ps (inset, **Figure 1(a)**).

The high pulse-energies of up to 5 mJ and tight-focusing conditions often used in $[AuCl_4]^-$ reduction experiments [14–21] produce peak intensities that significantly exceed the OB threshold. For instance, irradiation with 1 mJ pulses under the conditions described above results in a peak electron-density that surpasses the OB threshold by at least factor of 50 and even exceeds the maximum electron-density of 4×10^{22} cm^{-3} achievable in liquid water [42] for shorter pulses (dotted line, **Figure 1(b)**). Thus, to model the availability of electrons for $[AuCl_4]^-$ reduction, it is of primary importance to estimate the plasma volume in which the electron-density exceeds the OB threshold. The plasma volume may be estimated by calculating the critical distance z_{crit} in front of the focus where the OB threshold is exceeded. The value of z_{crit} for a given pulse energy, duration, and focusing-geometry may be calculated by solving Eq. (2) for a Gaussian beam in Eq. (1) at a series of propagation distances $z < 0$ cm (i.e., before the focal spot at $z = 0$ cm) in order to determine the highest electron density achieved. The resulting peak electron-density as a function of z is shown for the series of 1 mJ pulses from **Figure 1(b)** in **Figure 1(c)**. As the pulse duration decreases, OB begins farther from the focus, with z_{crit} increasing from 0.1 cm for 36 ps pulses to 0.3 cm for 30 fs pulses. This result shows that the plasma volume, which is proportional to z_{crit}^3, depends strongly on both pulse energy and duration in a given experiment. Our earlier simulations have shown that for a series of pulse durations with the same focusing-geometry, z_{crit} grows with peak-intensity as $z_{crit} \propto I^{1/2}$, meaning that the plasma volume grows as $I^{3/2}$ [16]. As discussed below, the growth of plasma volume is directly proportional to the $[AuCl_4]^-$ reduction rate.

2.2. Supercontinuum emission and filamentation

The filamentation process leading to SCE arises from self-focusing of the laser pulse in a nonlinear Kerr medium. A full discussion of the details of nonlinear light propagation leading self-focusing is beyond the scope of this work and may be found in Refs. [35–37]. Briefly, filamentation depends on the laser power P and is initiated when P exceeds the critical power P_{crit} [37, 43]

$$P_{\text{crit}} = \frac{3.77\lambda^2}{8\pi n_0 n_2} \tag{3}$$

where λ is the laser's wavelength, n_0 is the refractive index of the medium, and n_2 characterizes the intensity-dependent refractive index $n = n_0 + n_2 I$. In water, P_{crit} has been measured at 4.2×10^6 W for 800 nm pulses [44], which translates into very modest pulse energies of 0.13 and 0.42 μJ at 30 and 100 fs. Filamentation causes spectral broadening to both the red and blue of the laser wavelength. A red-shift is caused by rotational and vibrational motion of the molecules in the medium, and a blue-shift happens when the power P is high enough to form a shockwave at the trailing temporal edge of each pulse [36]. Blue-shifts produce a broad pedestal as far as 400 nm in the output-spectrum for pulses shorter than 100 fs [16, 27, 28, 35–37, 45] (see also **Figure 2**). Because SCE depends on power instead of peak intensity, filamentation may occur at intensities below the OB threshold; especially when the laser beam is weakly-focused or collimated [35–37, 45–49]. For laser beams with peak-intensities on the order of 10^{12} W cm^{-2}, the filament electron-density has been measured at $1 - 3 \times 10^{18}$ cm^{-3} [48, 49]. Such weakly-ionized SCE plasmas can drive $[AuCl_4]^-$ reduction even in the absence of OB [26–28], while the white light from the SCE has been shown to induce AuNP-fragmentation by resonant absorption and Coulomb explosion [45–47].

2.3. Experimental measurement of OB and SCE

The presence of OB and SCE may be measured with a spectrometer arranged as shown in **Figure 2(a)** [35, 36]. To detect OB from light that has scattered off of the OB plasma, the fiber mount is placed at a 90° angle to the laser beam (geometry (i) in **Figure 2(a)**) and a series of lenses focuses the light into the fiber mount. For SCE detection, the fiber mount is placed along the beam path, behind the sample (geometry (ii) in **Figure 2(a)**). A diffuser is attached to the fiber mount to avoid saturating the spectrometer. For tightly focused beams, OB is expected at any pulse duration, and SCE may also be present if the pulse is short. When the beam is loosely-focused or collimated, only SCE is expected.

To illustrate the conditions in which OB, SCE, or both are present, tightly focused pulses [16] and unfocused, collimated pulses [28] were measured using the setup in **Figure 2(a)**. **Figure 2(b)** shows spectra obtained at detector (i) for tightly focused 30 and 1500 fs pulses at 0.3 and 0.03 mJ pulse energy. The broadened spectrum for 30 fs pulses indicates the presence of SCE

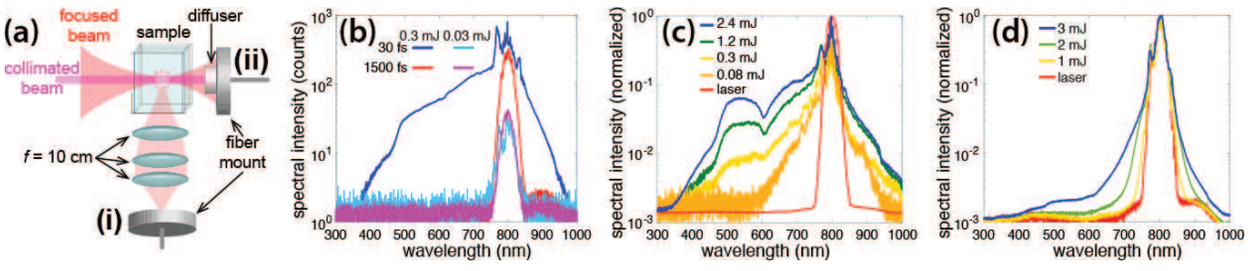

Figure 2. (a) Setup for OB and SCE measurements. (b) OB spectra for tightly focused 30 fs and 1500 fs pulses. (c) SCE spectra for tightly focused 30 fs pulses. (d) SCE spectra for collimated 30 fs pulses.

along with OB, while the narrow spectrum with 1500 fs pulses indicates that no SCE occurs. **Figure 2(c)** and **(d)** show SCE spectra obtained for 30 fs pulses at a series of pulse energies for tightly focused and collimated pulses. Under both conditions, asymmetric broadening towards the visible region of the spectrum grows with increasing pulse energy. The spectral broadening saturates for tightly focused pulses at energies above 1.2 mJ (**Figure 2(c)**), while greater pulse-energies would be needed to saturate the spectral width for unfocused pulses (**Figure 2(d)**). No OB is observed when the beam is collimated, indicating that a low-density plasma (LDP) with $\rho_e \sim 10^{18}$ cm^{-3} is present in the filaments [48, 49]. LDP conditions have been used by research groups to control the synthesis of AuNPs [26, 28, 45, 50].

3. Mechanisms of $[AuCl_4]^-$ reduction

3.1. Reactions of water

The key role that water photolysis plays, in the photochemical reduction of $[AuCl_4]^-$ and other metal salts, is well-established [14–22, 26, 27], and supported by the presence of H_2, O_2, and H_2O_2 as water is irradiated with high-intensity femtosecond laser pulses [14, 19, 51]. Two common mechanisms proposed to explain the reduction of aqueous $[AuCl_4]^-$ under high-intensity laser irradiation are (a) direct homolysis of the Au-Cl bond by multiphoton absorption to form Au(II) and Au(I) intermediates, and (b) chemical reduction of Au(III) ions by the reactive species formed from water photolysis [15–19, 26]. Since the number of water molecules far surpasses the number of $[AuCl_4]^-$ molecules in solution, the second proposed mechanism is more likely for $[AuCl_4]^-$ reduction to Au(0) in aqueous solutions. The photolysis reactions involved include [27, 52–55]

$$H_2O \xrightarrow{nh\nu} e^- + H^+ + OH. \tag{4}$$

$$e^- \longrightarrow e^-_{aq} \tag{5}$$

$$e^-_{aq} + OH\cdot \longrightarrow OH^- \tag{6}$$

$$H_2O \xrightarrow{nh\nu} H\cdot + OH. \tag{7}$$

$$2OH\cdot \longrightarrow H_2O_2 \tag{8}$$

$$H\cdot + H_2O \longrightarrow H_3O^+ + e^-_{aq}. \tag{9}$$

Although both hydrated-electrons and hydrogen radicals are capable of reducing $[AuCl_4]^-$, the fast consumption of H. via Eq. (9) observed in water photolysis using picosecond pulses [53] suggests an inconsequential contribution by H. to $[AuCl_4]^-$ reduction. In contrast, hydrated electrons may be formed from both the free electrons generated in OB plasma via Eq. (5) within several hundred femtoseconds [54, 55], and from the reaction of water with H. via Eq. (9). Hydrated electrons have lifetimes of up to hundreds of nanoseconds in pure water [56] and

react with $[AuCl_4]^-$ with a diffusion-controlled rate constant of 6.1×10^{10} M^{-1} s^{-1} [57]. Therefore, hydrated electrons are the dominant $[AuCl_4]^-$ reducing agent through the reaction [27]

$$[AuCl_4]^- + 3e^-_{aq} \rightarrow Au(0) + 4Cl^-. \tag{10}$$

Another product of water photolysis, H_2O_2, is generated from the recombination of two hydroxyl radicals via Eq. (8) and drives $[AuCl_4]^-$ reduction and AuNP formation [15, 16, 19, 20]. Tangeysh et al. explored the role that H_2O_2 played in $[AuCl_4]^-$ reduction by monitoring the UV–vis absorbance of $[AuCl_4]^-$ samples after laser-irradiation termination, but before all of the $[AuCl_4]^-$ had been consumed [19]. They explained the post-irradiation $[AuCl_4]^-$ reduction and SPR absorbance-peak growth by proposing that the H_2O_2 produced during irradiation reduced the remaining $[AuCl_4]^-$, in the presence of the existing AuNPs [19]. This hypothesis was developed further by Tibbetts et al. [15], using previous work showing that H_2O_2 reduces $[AuCl_4]^-$ in the presence of AuNPs via the reaction [58, 59]

$$[AuCl_4]^- + \frac{3}{2}H_2O_2 + Au_m \rightarrow Au_{m+1} + \frac{3}{2}O_2 + 3HCl + Cl^-, \tag{11}$$

where the existing AuNPs act as a catalyst for $[AuCl_4]^-$ reduction. This process underlies the observed autocatalytic reduction kinetics of $[AuCl_4]^-$.

3.2. Kinetics

Controlling the sizes and shapes of AuNPs starts with kinetic control of their nucleation and growth. LaMer's nucleation theory, developed in 1950 [60], was used to describe AuNP formation first [4, 9, 61], but Turkevich's studies [62] on reduction of $HAuCl_4$ using sodium citrate yielded more appropriate AuNP formation-mechanisms, including autocatalysis [62–64] and aggregative growth [65, 66]. In 1997, Watzky and Finke described the reduction of transition metal salts using H_2, undergoing slow, continuous nucleation accompanied by fast, autocatalytic surface growth to form nanoparticles. They described this mechanism using a quantitative, two-step rate law [67],

$$-\frac{d[A]}{dt} = \frac{d[B]}{dt} = k_1[A] + k_2[A][B] \tag{12}$$

where [A] is the precursor (metal salt) concentration, [B] is the metal nanoparticle concentration, k_1 is the rate constant of metal-cluster nucleation (slow) and k_2 is the rate constant of autocatalytic growth of the nanoparticles (fast) [67, 68]. Integration of Eq. (12) gives the time-dependent precursor and metal nanoparticle concentrations [A(t)] and [B(t)] [67]

$$[A(t)] = \frac{\frac{k_1}{k_2} + [A(0)]}{1 + \frac{k_1}{k_2[A(0)]}e^{(k_1 + k_2[A(0)])t}} \tag{13}$$

$$[B(t)] = 1 - \frac{\frac{k_1}{k_2} + [A(0)]}{1 + \frac{k_1}{k_2[A(0)]}e^{(k_1 + k_2[A(0)])t}} \tag{14}$$

where [A(0)] is the initial precursor concentration. The rate law in Eq. (13) has been used to describe AuNP formation from reducing ionic precursors via wet chemical routes [67–69] and for femtosecond laser-induced $[AuCl_4]^-$ reduction under a variety of laser conditions and solution compositions [15, 16, 26, 28]. Eq. (14) follows if it is assumed that the conversion of Au(III) to Au(0) is fast enough that no significant concentration of intermediate species like Au(I) builds up.

The time-dependent concentrations of $[AuCl_4]^-$ and AuNPs needed to determine the reaction kinetics may be obtained from *in situ* UV–vis spectra recorded during laser irradiation [15]. **Figure 3(a)** displays representative absorbance spectra of $[AuCl_4]^-$ after different irradiation times. The arrow labeled 250 nm corresponds to the decrease in the LMCT band of $[AuCl_4]^-$, while the arrow labeled 450 nm corresponds to the growth of AuNPs [15, 16, 70]. To obtain the time-dependent $[AuCl_4]^-$ concentration in Eq. (13), the absorbance of $[AuCl_4]^-$ is monitored at λ = 250 nm. Because AuNPs also absorb across the UV range, the absorbance at 250 nm corresponds to the absorbance contributions from both the $[AuCl_4]^-$ precursor and AuNP product species. The $[AuCl_4]^-$ contribution can be isolated from the 250 nm absorbance by subtracting off the AuNP contribution, as described in previous work [15, 16]. Alternatively, monitoring the absorbance at $\lambda = 450$ nm where only the AuNPs absorb [70] allows direct monitoring of the - time-dependent AuNP growth. Both representations of the reaction kinetics are shown in **Figure 3**: (b) normalized absorbance of $[AuCl_4]^-$ at 250 nm and (c) 450 nm as a function of laser irradiation time for focused 30 fs laser pulses at a series of pulse energies [16]. The dots denote the experimental data, and the solid lines are fits to Eq. (13) (**Figure 3(b)**) or Eq. (14) (**Figure 3(c)**). The disappearance rate of $[AuCl_4]^-$ and growth rate of AuNPs mirror each other, showing that the rate constants may be extracted from fitting either spectral absorbance. In practice, small amounts of intermediate species such as Au(I) are present during photochemical reduction [15], so the rate constants extracted from fitting the normalized 450 nm absorbance to Eq. (14) are $20 - 50\%$ lower than those from fitting the normalized 250 nm absorbance to Eq. (13).

Under certain experimental conditions where the $[AuCl_4]^-$ reduction rate is slowed, the experimental kinetics are more accurately modeled by adding a linear component to Eq. (13) [15, 28],

$$[A(t)] = \frac{\frac{k_1}{k_2} + [A(0)]}{1 + \frac{k_1}{k_2[A(0)]} e^{(k_1 + k_2[A(0)])t}} - k_3 t \tag{15}$$

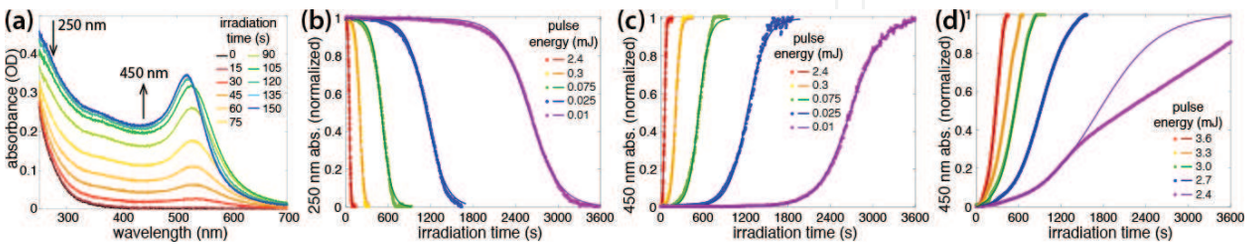

Figure 3. (a) UV–vis spectra of $[AuCl_4]^-$ solution irradiated for different times. Representative plots of normalized absorbance at 250 nm (b) and 450 nm (c), (d) (dots) as a function of irradiation time for the pulse energies labeled in the legend, with fits to Eq. (13) (b), Eq. (14) (c), and Eq. (16) (d) (solid lines). Data taken from refs. [16, 28].

$$[B(t)] = 1 - \frac{\frac{k_1}{k_2} + [\mathrm{A}(0)]}{1 + \frac{k_1}{k_2[\mathrm{A}(0)]} e^{(k_1 + k_2[\mathrm{A}(0)])t}} + k_3 t. \tag{16}$$

The third rate constant, k_3, is zeroth order with respect to the $[AuCl_4]^-$ concentration, and was suggested arise due to limited availability of reducing species from photolysis of the solvent [15]. This rate equation more accurately fits the reduction kinetics when the laser beam is collimated such that LDP conditions are present [28], as shown in **Figure 3(d)**. When the pulse energy is sufficiently low (2.4 mJ), the AuNP growth was significantly slower due to agglomeration of the formed nanoparticles; therefore, only the first portion of the experimental data was fit to Eq. (16). Similar agglomeration has been observed in other experiments conducted under LDP conditions, in which the initial portion of experimental data was fit to Finke-Watsky kinetics [26].

Extracting the rate constants at a series of experimental conditions (e.g., solution pH [15], pulse energy [16, 28]) provides significant insight into the roles that the reactions in Eqs. (4)–(9) play in the conversion of $[AuCl_4]^-$ to AuNPs. **Figure 4(a)** and **(b)** show the rate constants k_1 and k_2 extracted from fits to Eqs. (13) and (16), respectively, for tightly focused and collimated 30 fs pulses, as a function of pulse energy (proportional to peak intensity I) [16, 28]. In the log–log plots, the slopes of the least squares fit lines denote the power law dependence of each rate constant on the peak intensity. For the tight focusing geometry in **Figure 4(a)**, the nucleation rate constant grows as $k_1 \sim I^{(1.6\pm0.2)}$, a factor of three faster than the growth of the autocatalytic rate constant $k_2 \sim I^{(0.56\pm0.02)}$. In contrast, under LDP conditions, k_1, k_2, and k_3 all grow approximately as I^4 (**Figure 4(b)**).

The power law dependence of k_1 under tight-focusing conditions corresponds to the growth of the OB plasma volume V with peak-intensity I as $V \sim I^{1.5}$ calculated via Eq. (2) (c.f., Section 2.1) [16]. **Figure 4(c)** shows that $k_1 \sim V$ for pulse durations ranging from 30 to 1500 fs under tight-focusing conditions. This result demonstrates the that the production of hydrated electrons an OB plasma controls the rate of nucleation of $[AuCl_4]^-$. The higher sensitivity of $k_1 \sim I^4$ under LDP conditions [28] is consistent with the electron density in LDP conditions being proportional to the multiphoton order required for ionization of the medium [37], where 5 photons at 800 nm are needed to ionize water [34]. The importance of hydrated electrons to

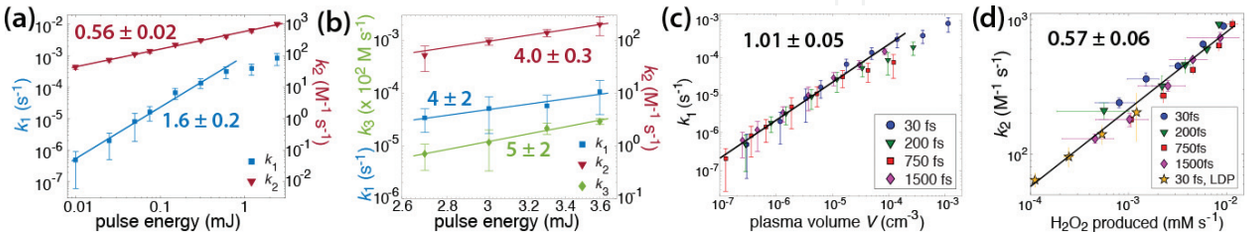

Figure 4. Rate constants for 30 fs laser pulses (blue, k_1; red, k_2; green k_3) as a function of pulse energy for (a) tight focusing geometry and (b) LDP geometry. (c) Correlation between k_1 rate constant and calculated OB plasma volume for tight focusing geometry. (d) Correlation between k_2 rate constant with H_2O_2 production for tight focusing and LDP geometries. Data taken from refs. [16, 28].

$[AuCl_4]^-$ reduction has been demonstrated in two other works [15, 26]. The addition of N_2O as a hydrated electron scavenger to aqueous $[AuCl_4]^-$ significantly lowers the value of k_1 in Eq. (14) with respect to k_2, thereby isolating the contribution of hydrated electrons to $[AuCl_4]^-$ nucleation [26]. Increasing the solution pH of aqueous $[AuCl_4]^-$ through addition of KOH significantly increases k_1 [15], which is consistent with previous findings that the lifetimes of hydrated electrons are suppressed in acidic solution [55].

Under both tight-focusing and LDP conditions, the power law dependence of k_2 corresponds to the formation rate of H_2O_2 from water. Under tight-focusing conditions, the formation rate of H_2O_2 is $[H_2O_2] \sim I$, so the lower dependence of $k_2 \sim I^{1/2}$ results in the relationship $k_2 \sim [H_2O_2]^{1/2}$ [16]. The same correlation was found under LDP conditions, where the formation rate of H_2O_2 is $[H_2O_2] \sim I^8$ and $k_2 \sim I^4$ [28]. Both correlations between $[H_2O_2]$ and k_2 are shown in **Figure 4(d)**. These results are consistent with other work in which the addition of the OH. scavenger 2-propanol [26] resulted in increased k_1 values relative to k_2 values and slower growth of AuNPs.

The kinetics results quantifying the dependence of both nucleation and autocatalytic growth rate constants demonstrate the importance of both short and long-lived reducing species to control the formation of AuNPs via photochemical reduction of aqueous $[AuCl_4]^-$. The reactive species produced during water photolysis can be controlled by changing both the laser irradiation conditions [16, 28] and the chemical composition of the $[AuCl_4]^-$ solution [15, 26]. The following section will review how changing both of these reaction conditions can control the size and shape of the synthesized AuNPs.

4. Controlling Au nanoparticle sizes

Several recent articles have reported some degree of control over the size of AuNPs synthesized by photochemical reduction of $[AuCl_4]^-$ through the manipulation of experimental conditions: broadly, the laser parameters and solution composition. The focusing-geometry, pulse energy, and pulse duration determine the generation of OB and SCE, which direct AuNP growth [16, 20, 28]. Adding scavengers and modifying the solution pH also change the $[AuCl_4]^-$ reduction kinetics, and therefore, particle size [15, 26]. Finally, adding capping can produce smaller AuNPs [14, 19, 20, 29, 30].

4.1. Laser parameters

4.1.1. Focusing-geometry

Focusing-geometries influence the nature of the nonlinear interactions between the laser and solution (c.f., Section 2). Without strong-focusing, SCE yields a LDP environment containing electron-densities on the order of $\rho_e \sim 10^{18}$ cm^{-3}. This setup has been used for photochemical $[AuCl_4]^-$ reduction [26, 28] experiments and Au ablation [45, 50] experiments. LDP conditions seem well-suited to applications like AuNP synthesis, because second-order reactions are

suppressed, including those that yield H_2O_2 [26, 50]. Without abundant reducing species, $[AuCl_4]^-$ to AuNP conversion is slow. Many research groups opt to use a focused-geometry [14–20], which yield electron densities that exceed the OB threshold, $\sim 10^{20}$ cm^{-3}. Low numerical aperture (NA) geometries produce SCE through self-focusing and filamentation processes. These processes can cause intensity-clamping, which stops the intensity from exceeding $I \sim 10^{13}$ W cm^{-2} [37], and limits the number of reactive species available for reduction [20]. In contrast, tight-focusing (high-NA) geometries, simultaneous spatial and temporal focusing (SSTF) [71], or spatial beam-shaping [72] can avoid excessive filamentation and intensity clamping. In Au nanoparticle synthesis, tight-focusing [14, 16, 18] and SSTF [15, 19, 20], where the frequency components of the laser pulse are spatially separated prior to focusing, have both been used for this purpose. **Figure 5** shows schematic diagrams (top) and photographs (bottom) of fs-laser irradiation of water using (a) collimated beam geometry [28], (b) low-NA focusing [20], (c) high-NA focusing [16], and (d) SSTF [19]. The absence of visible filaments in panels (c) and (d), compared to (b), suggest less intensity-clamping, and so a higher peak-intensity at the focal spot.

Another phenomenon to consider when experimenting with focusing-conditions is cavitation bubble formation, which happens when the OB electron-density threshold is exceeded [38]. The generated cavitation bubbles are sensitive to the shape of the laser-plasma [20, 72]. Under low-NA focusing-conditions with filamentation and SCE, the bubbles are ejected from the focus with low kinetic energy, seen as a small stream of bubbles rising from the center of the cuvette in **Figure 5(b)**. This condition results in inefficient and asymmetrical mixing-dynamics of the reactive species throughout the solution, but can be improved with the addition of a magnetic stir-bar [20]. Similarly, a stir bar is needed when operating under LDP conditions to ensure that the solution is being mixed [26, 28]. Both high-NA focusing and SSTF produce more spherical plasmas, which eject high kinetic energy bubbles into solution radially [72], causing turbulent mixing of the reactive species into the solution (evident in **Figure 5(c)**) and removing the need for stirring [16, 20].

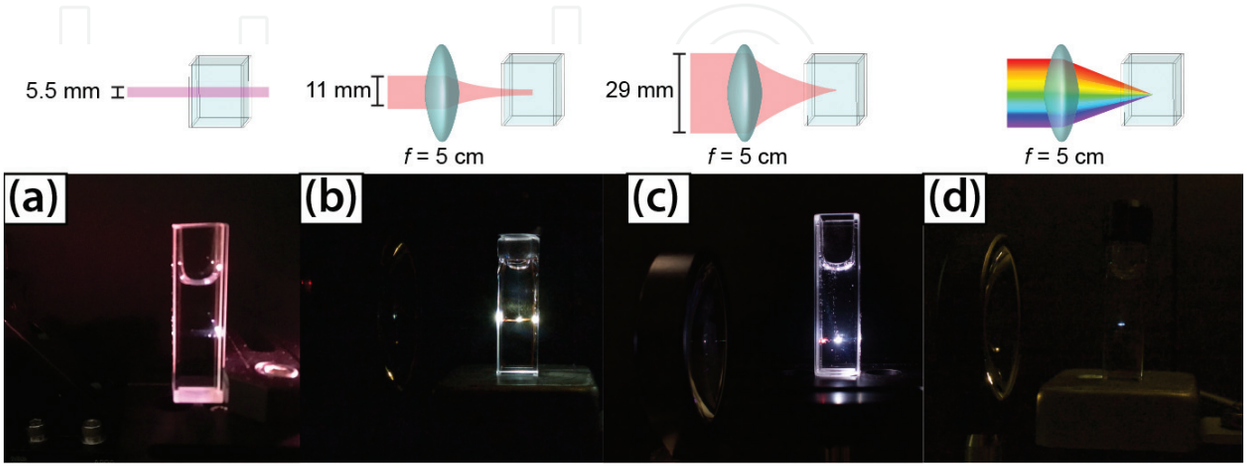

Figure 5. Diagrams (top) and photographs (bottom) of irradiated water using (a) collimated beam, (b) low-NA focusing, (c) high-NA focusing, and (d) SSTF.

Ref.	Condition	Energy (mJ)	Size (nm)
[26]	LDP	1.35	29.1 ± 17.3
[28]	LDP	2.7	27.1 ± 7.0
[20]	Low-NA	1.8	13.6 ± 8.0
[18]	High-NA	5.6	4.0 ± 1.7
[16]	High-NA	2.4	3.5 ± 1.9
[20]	SSTF	1.8	10.2 ± 4.1
[15]	SSTF	2.5	9.2 ± 4.1

Table 1. Reported laser focusing conditions and resulting AuNP sizes.

The complex interactions between high-intensity fs laser pulses and aqueous solution result in the particle size being sensitive to different focusing-conditions. **Table 1** summarizes the results of AuNP syntheses prepared in aqueous solutions without capping agents across focusing conditions. Of the reported sizes, the largest AuNPs resulted from the LDP conditions [26, 28], which limits production of the reducing species, driving AuNP formation through aggregative growth and agglomeration. Smaller AuNPs were formed with the high-NA focusing conditions [16, 18], which produces high electron-densities because of tight laser-focus; filamentation is suppressed, and the reducing species (electrons and H_2O_2) are thoroughly mixed throughout the solution by the OB plasma. In combination, these conditions generate many Au(0) seeds but limit Au(III) ions. SSTF and low-NA focusing-geometries create intermediate AuNP sizes. The SSTF focusing-geometry improves size-distribution because it mixes the reactive species well with its spherical plasma [20]. Adjusting the laser's focus-geometry has a strong influence on both the production rate and spatial distribution of the reducing species required for AuNP formation, and yields another dimension of control over particle sizes.

4.1.2. Pulse energy and duration

Several studies on focusing-conditions have demonstrated that increasing the pulse energy reduces AuNP size [16, 20, 28]. When tight-focusing geometry was used, increasing the energy of a 30 fs pulse from 0.15 mJ to 2.4 mJ decreased AuNP size from 6.4 ± 5.6 nm to 3.5 ± 1.9 nm [16] (**Figure 6(a)** and **(b)**). This trend was also seen when LDP conditions were used: increasing the energy of 30 fs pulses from 2.7 to 3.3 mJ reduced AuNP size from 27 ± 7 to 14 ± 6 nm [28] (**Figure 6(c)** and **(d)**). These results are consistent with earlier reports using SSTF with 36 ps pulses to irradiate solutions of $[AuCl_4]^-$ and polyethylene glycol (PEG), a capping agent. Increasing the pulse energy from 0.45 mJ to 1.8 mJ reduced the average particle size from 9.6 ± 2.7 to 5.8 ± 1.1 nm [20].

While the pulse energy strongly influences the size of the AuNPs from photochemical reduction of $[AuCl_4]^-$, the pulse duration, or linear frequency chirp, has at most a modest effect on the AuNP size at a fixed pulse energy and focusing condition [16, 20]. Under tight focusing conditions, stretching the pulse duration was stretched from 30 to 1500 fs (negatively chirped) at a 0.15 mJ pulse energy slightly decreased the AuNP sizes from 6.4 ± 5.6 to 4.4 ± 4.0 nm [16].

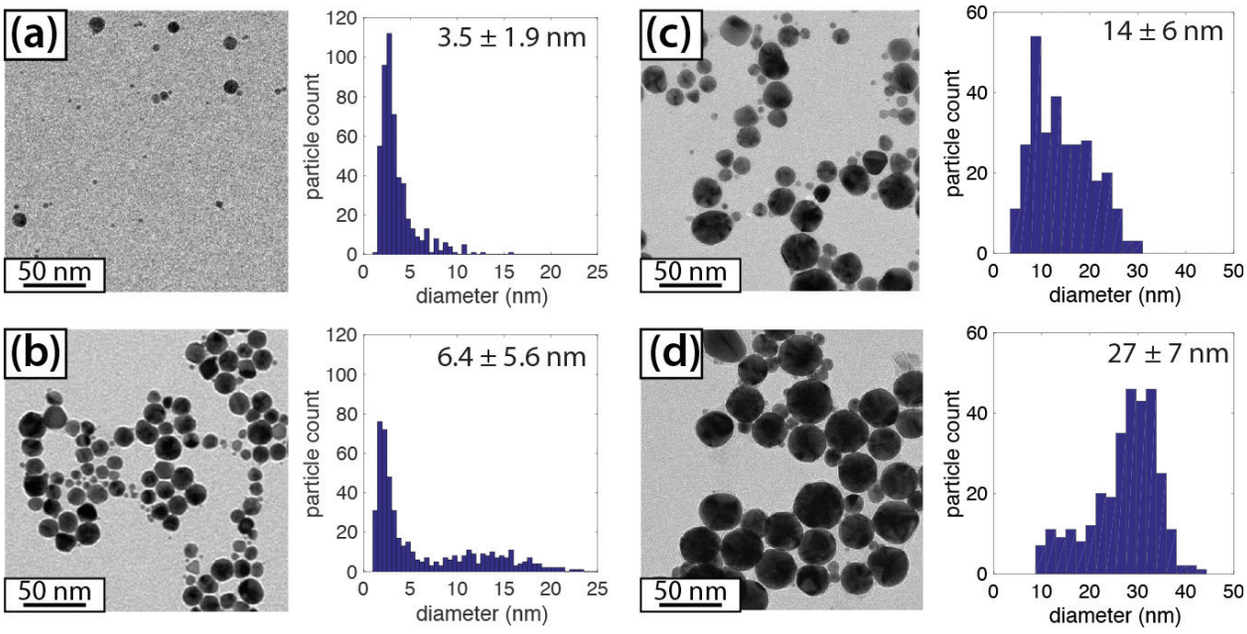

Figure 6. Representative TEM images and AuNP size distributions synthesized with 30 fs pulses under the following conditions: (a) tightly focused, 2.4 mJ; (b) tightly focused, 0.15 mJ; (c) LDP, 3.3 mJ; and (d) LDP, 2.7 mJ.

When the experiment was repeated at a high pulse energy (2.4 mJ), the AuNP size increased from 3.5 ± 1.9 nm for 30 fs pulses to 6.3 ± 2.4 nm for 1500 fs pulses [16]. In a separate experiment using low-NA focusing conditions, 1.8 mJ pulses with chirp coefficients of $+20,000$ fs^2, 0 fs^2, and $-20,000$ fs^2 (corresponding to 35 fs unchirped pulses and 2 ps chirped pulses) produced 8.2 ± 3.5, 8.1 ± 3.4, and 8.1 ± 6.5 nm AuNPs, respectively [20]. Collectively, these results suggest that that for sufficiently high peak intensities generating OB conditions, the pulse duration does not significantly affect the size of AuNPs produced by photochemical reduction of $[AuCl_4]^-$.

4.2. Chemical composition

4.2.1. Scavengers

Water photolysis produces reactive species, which govern $[AuCl_4]^-$ reduction and therefore AuNP formation. To manage particle growth, radical scavengers can be added to solution. As summarized in Section 3, it is primarily the hydrated electrons that reduce $[AuCl_4]^-$ (Eq. (10)). H_2O_2 (formed by the recombination of two hydroxyl radicals (Eq. (8)), facilitates autocatalytic particle growth (Eq. (11)). Scavengers can selectively hinder the production of water photolysis byproducts such as H_2O_2 [73], so they have been used to control reduction kinetics [26].

The hydrated-electron scavenger N_2O, and hydroxyl radical scavengers 2-propanol and ammonia, were originally studied in water radiolysis using X-rays and γ rays [74]. More recently, they have been used to control the photochemical synthesis of Au and Ag nanoparticles in femtosecond-laser plasmas [21, 26, 73, 75]. The addition of N_2O to aqueous $[AuCl_4]^-$ is expected to limit the availability of hydrated electrons and slow the $[AuCl_4]^-$ reduction rate, forming fewer Au(0) nuclei in solution. This situation would result in a significant number of Au(III) ions being reduced on the surface of the Au(0) nuclei in the presence of H_2O_2, promoting the surface-

mediated autocatalytic growth into larger AuNPs. In contrast, the addition of a hydroxyl radical scavenger such as 2-propanol should not only limit the production of H_2O_2 via Eq. (8), but also prevent the quenching of hydrated electrons via Eq. (6). As a result, $[AuCl_4]^-$ reduction should be fast and autocatalytic AuNP growth should be limited, resulting in smaller AuNPs. These predictions have been laid out in recent literature [21, 26].

Belmouaddine et al. [26] investigated the effect of adding N_2O or 2-propanol to aqueous $[AuCl_4]^-$ solutions they irradiated with 1.35 mJ, 112 fs pulses. They monitored the reduction kinetics to determine the k_1 and k_2 rate constants in Eq. (13). By comparing the k_2/k_1 ratios obtained in the two scavenger experiments, they were able to relate each scavenger to its role in the reduction and autocatalytic growth processes. In the presence of the hydrated-electron scavenger N_2O, the k_2/k_1 ratio was two orders of magnitude higher than it was when the radical scavenger 2-propanol was used. This is consistent with the dependence of k_1 and k_2 on hydrated-electrons and H_2O_2, discussed in Section 3. The resulting AuNPs synthesized in the presence of N_2O and 2-propanol were 54.4 ± 9.8 nm, and 28.5 ± 5.9 nm. These results are consistent with the predictions that (1) slow nucleation and significant autocatalytic growth in the presence of N_2O will produce large AuNPs, and (2) fast nucleation and limited autocatalytic growth in the presence of 2-propanol will produce small AuNPs.

In another study, Uwada et al. [21] investigated the effects of alcohols (1-propanol, 2-propanol, ethanol) on aqueous $[AuCl_4]^-$ solutions irradiated with 120 fs pulses, using a series of pulse energies from 1 to 50 μJ. At low pulse energies, with intensity below 7×10^{15} W cm^{-2}, no AuNPs formed if there were no alcohols. AuNP size-dependence on the pulse energy followed the *opposite* trend to that observed in Refs. [16, 20] and discussed in Section 4.1.2: the AuNPs formed in solutions containing 1-propanol increased in diameter from 24 to 37 nm when the intensity increased from 2×10^{15} to 7×10^{15} W cm^{-2} [21]. The authors proposed that the alcohol radicals formed from the OH. scavenging reaction

$$ROH + OH\cdot \rightarrow RO\cdot + H_2O \tag{17}$$

act as the primary reducing agents of $[AuCl_4]^-$ at low laser intensities where few hydrated electrons are formed. These results suggest that radical scavengers not only manage the AuNP size, but also boost photochemical reduction of $[AuCl_4]^-$ into AuNPs at lower laser intensities by providing an additional free-radical reducing agent.

4.2.2. pH

Changing the pH of irradiated aqueous $[AuCl_4]^-$ solutions by adding either HCl or KOH affects both the reduction kinetics and the resulting AuNP sizes [15]. Solution pH is well known to affect Au(III) complex speciation: $[AuCl_4]^-$ dominates under acidic conditions, $\left[Au(OH)_4\right]^-$ dominates under basic conditions, and mixtures of $\left[AuCl_x(OH)_{4-x}\right]^-$, $x = 1 - 3$, species exist under neutral conditions [76, 77]. Different complex stabilities were thought to be the driving force for Au(III) reduction with chemical reducing agents, where $\left[Au(OH)_4\right]^-$ was less reactive because of stronger Au-OH bonds, compared to Au-Cl bonds [76, 77]. With increasing pH, as solution was irradiated with 36 ps, 2.5 mJ pulses under SSTF focusing conditions, the

reverse trend occurred, and higher $[AuCl_4]^-$ reduction rates formed smaller AuNPs [15]. At low pH, the hydrated-electron lifetime is reduced [55] and H_2O_2 oxidizes AuNPs [78], causing a slow $[AuCl_4]^-$ reduction rate that produced large, polydisperse 19.4 ± 7.1 nm AuNPs (at pH 2.5). When pH was higher (pH 5.4), the hydrated-electron lifetime is longer [55] and the oxidation potential of H_2O_2 increases as it is deprotonated to HO_2^- [59], leading to faster reduction of $[AuCl_4]^-$ and small AuNPs with size distributions of 4.8 ± 1.9 nm. Slightly larger 6.6 ± 3.1 nm AuNPs were formed at pH 8.4 due to the acceleration of the autocatalytic growth rate constant k_2 in Eq. (13).

For comparison with the results in Ref. [15], experiments performed in our laboratory using the tight-focusing conditions in Ref. [16] also showed that the AuNP size depends on solution pH. Aqueous solutions (0.1 mM $KAuCl_4$) with varying amounts of KOH (up to 0.75 mM, pH 4.0–9.3) were irradiated with 50 μJ, 30 fs pulses for 10–33 min, sufficient to convert all $[AuCl_4]^-$ to AuNPs. The UV–vis spectra recorded when the conversions of $[AuCl_4]^-$ to AuNPs were completed are shown in **Figure 7(a)**. As the solution pH increases, the SPR feature blue-shifts and decreases in intensity, indicating the production of smaller AuNPs [70]. TEM analysis of the AuNPs synthesized at pH 4.0, 5.2, and 9.3 (**Figure 7(b)–(d)**) agreed. At pH 4.0, there is a distinct bimodal size-distribution, with a number of small (< 4 nm) AuNPs and a broad distribution of particles to as large as 65 nm. As a result, a meaningless statistical size-distribution of 8.6 ± 12.4 nm is obtained. At pH 5.2, there is a bimodal distribution centered at 3 and 18 nm, with a size-distribution of 8.6 ± 6.7 nm. The most monodisperse AuNPs are seen at pH 9.3, with a size-distribution of 9.2 ± 4.5 nm. The slightly larger average AuNP size is because there are very few < 4 nm particles compared to what had been seen at lower pH. This absence of extremely small particles is likely due to the high concentration of H_2O_2 produced in the plasma, as discussed in Ref. [15].

4.2.3. Capping agents

One of the most widely used strategies for controlling AuNP size during chemical synthesis is the addition of capping agents, including polymers and surfactants, to stop particle growth [2]. Increasing the molar ratio of a capping agent to Au(III) salt typically results in smaller AuNPs in chemical syntheses [79]. A similar trend is observed for femtosecond laser-based syntheses of AuNPs, as shown in **Table 2**. Nakamura et al. [14] found that addition of polyvinylpyrrolidone (PVP) to aqueous $HAuCl_4$ decreased AuNP size and gave a tighter size-distribution,

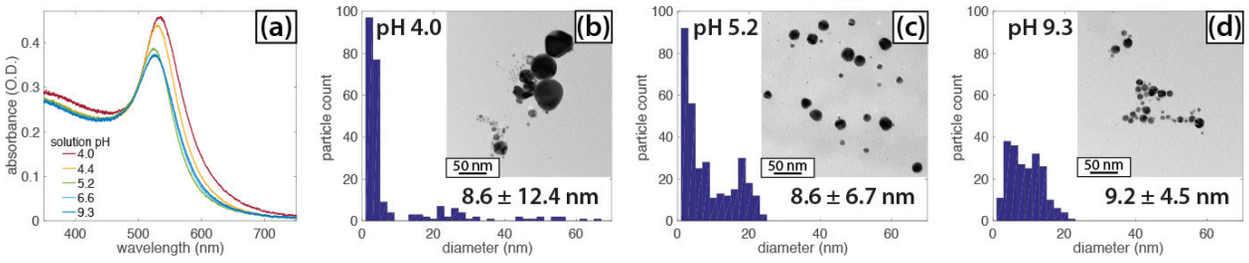

Figure 7. UV-vis spectra (a) and TEM images with size distributions (b)–(d) of AuNPs synthesized at different solution pH using the experimental setup in ref. [16].

Ref.	Laser condition	Capping agent	Capping agent: Au	Size (nm)	Size range (nm)
[14]	High-NA	PVP[a]	0.001	2, 7	1 – 77
			0.01	4.5	1 – 17
			0.1	3	2 – 7
[19]	SSTF	PEG_{45}	0.05	11 ± 2.4	5 – 18
			0.1	6.0 ± 1.4	3 – 11
			0.25	3.9 ± 0.7	2 – 7
			0.5	4.1 ± 0.8	2 – 7
[45]	Ablation,	Dextran[b]	0.0002	76 ± 19	
	Low-NA		0.002	30 ± 6	
			0.007	8.5 ± 1.7	
			0.05	3.0 ± 0.8	
			0.2	3.7 ± 1.1	

[a]Median size estimated from reported histogram.
[b]Standard deviation values estimated from 20 to 30% reported.

Table 2. Capping agents effect on AuNP size.

up to a 0.1:1 PVP:Au ratio. Tangeysh et al. [19] used poly(ethylene glycol) (PEG_{45}, $n = 45$) and found an optimal PEG_{45}:Au ratio of 0.25:1. The same trend is observed when femtosecond pulses are used to ablate an Au target [45], where the smallest particles made from irradiating AuNPs in solutions of varied dextran concentrations were optimized at a dextran:Au ratio of 0.05:1.

In addition to controlling AuNP size in femtosecond laser-based syntheses, capping agents like PEG_{45} [19], chitosan (a cationic polysaccharide) [29], and (2-hydroxyethyl) trimethylammonium glycinate ([HETMA][Gly], an ionic liquid) [30] accelerate the conversion of $[AuCl_4]^-$ to AuNPs. It was proposed that fragmentation of PEG_{45} in the laser-generated plasma produces alcohol radicals (analogous to Eq. (17)) that can reduce $[AuCl_4]^-$ and accelerate AuNP formation [19]. The formation of AuNPs in the presence of chitosan correlates with the oxidation of hydroxyl groups on the chitosan [29], indicating that the chitosan contributes to $[AuCl_4]^-$ reduction. The [HETMA][Gly] forms a complex with $[AuCl_4]^-$, which facilitated its reduction under OB conditions with tight-focusing [30]. These results suggest the potential of selective control over both $[AuCl_4]^-$ reduction kinetics and AuNP size through careful choice of capping agents and their concentrations.

5. Conclusion

Photochemical reduction of $[AuCl_4]^-$ using femtosecond laser irradiation is a simple, green method for controlling the growth of AuNPs. This chapter presented a review of the physical and chemical mechanisms of aqueous $[AuCl_4]^-$ transformation to AuNPs, from the physical

processes occurring in plasma to AuNP size-control through selective tailoring of the solution composition. In Section 2, we discussed the physical processes of OB and SCE that occur because of ultrafast laser irradiation of water. The time-dependent electron density generated in OB plasma was modeled in relation to laser intensity, and the role that electrons play in $[AuCl_4]^-$ reduction were explained in Section 3. Reactive species produced in OB plasma were identified, and their roles in the kinetically controlled photochemical reduction of $[AuCl_4]^-$ (electrons $\propto k_1$) and surface-mediated autocatalytic growth into AuNPs (H_2O_2 production $\propto k_2$) were quantified and discussed. Finally, in Section 4, these approaches to control the size of AuNPs were reviewed. Both laser parameters (focusing-geometry, pulse energy, and duration) and solution modifications (pH, adding scavengers or capping agents) were discussed in how they affected the chemical system and reaction mechanism, allowing for size-control of AuNPs. Laser parameters and solution composition both play significant roles in the formation and resulting size of AuNPs, and this chapter highlights these considerations to direct future research.

Acknowledgements

This work was supported by the American Chemical Society Petroleum Research Fund under Grant no 57799-DNI10 and Virginia Commonwealth University.

Author details

Mallory G. John, Victoria Kathryn Meader and Katharine Moore Tibbetts*

*Address all correspondence to: kmtibbetts@vcu.edu

Department of Chemistry, Virginia Commonwealth University, Richmond, VA, USA

References

[1] Zhang JZ, Noguez C. Plasmonic optical properties and applications of metal nanostructures. Plasmonics. 2008;**3**:127

[2] Dreaden EC, Alkilany AM, Huang X, Murphy CJ, El-Sayed MA. The golden age: Gold nanoparticles for biomedicine. Chemical Society Reviews. 2012;**41**:2740

[3] Dreaden EC, Mackey MA, Huang X, Kang B, El-Sayed MA. Beating cancer in multiple ways using nanogold. Chemical Society Reviews. 2011;**40**:3391

[4] Bastús NG, Comenge J, Puntes V. Kinetically controlled seeded growth synthesis of citrate-stabilized gold nanoparticles of up to 200 nm: Size focusing versus ostwald ripening. Langmuir. 2011;**27**:11098

[5] Haynes CL, McFarland AD, Duyne RPV. Surface-Enhanced Raman Spectroscopy. Analytical Chemistry. 2005;**77**:338 A

[6] Alkilany AM, Lohse SE, Murphy CJ. The gold standard: Gold nanoparticle libraries to understand the nano-bio interface. Accounts of Chemical Research. 2013;**46**:650

[7] Mukherjee S, Libisch F, Large N, Neumann O, Brown LV, Cheng J, Lassiter JB, Carter EA, Nordlander P, Halas NJ. Hot electrons do the impossible: Plasmon-induced dissociation of H_2 on Au. Nano Letters. 2013;**13**:240

[8] Linic S, Christopher P, Ingram DB. Plasmonic-metal nanostructures for efficient conversion of solar to chemical energy. Nature Materials. 2011;**10**:911 dEP

[9] Xia Y, Xiong Y, Lim B, Skrabalak S. Shape-controlled synthesis of metal nanocrystals: Simple chemistry meets complex physics?. Angewandte Chemie, International Edition. 2009;**48**:60

[10] Personick ML, Mirkin CA. Making sense of the mayhem behind shape control in the synthesis of gold nanoparticles. Journal of the American Chemical Society. 2013;**135**:18238

[11] Zeng H, Du X-W, Singh SC, Kulinich SA, Yang S, He J, Cai W. Nanomaterials via laser ablation/irradiation in liquid: A review. Advanced Functional Materials. 2012;**22**:1333

[12] Svetlichnyi VA, Shabalina AV, Lapin IN, Goncharova DA. In: Yang D, editor. Metal oxide nanoparticle preparation by pulsed laser ablation of metallic targets in liquid. Applications of Laser Ablation - Thin Film Deposition, Nanomaterial Synthesis and Surface Modification. Rijeka: InTech; 2016 Chap. 11

[13] Sylvestre J-P, Poulin S, Kabashin AV, Sacher E, Meunier M, Luong JHT. Surface chemistry of gold nanoparticles produced by laser ablation in aqueous media. The Journal of Physical Chemistry B. 2004;**108**:16864

[14] Nakamura T, Mochidzuki Y, Sato S. Fabrication of gold nanoparticles in intense optical field by femtosecond laser irradiation of aqueous solution. Journal of Materials Research. 2008;**23**:968

[15] Tibbetts KM, Tangeysh B, Odhner JH, Levis RJ. Elucidating strong field photochemical reduction mechanisms of aqueous $[AuCl_4]^-$: Kinetics of multiphoton photolysis and radical-mediated reduction. The Journal of Physical Chemistry. A. 2016;**120**:3562

[16] Meader VK, John MG, Rodrigues CJ, Tibbetts KM. Roles of free electrons and H_2O_2 in the optical breakdown-induced photochemical reduction of aqueous $[AuCl_4]^-$. The Journal of Physical Chemistry. A. 2017;**121**:6742

[17] Zhao C, Qu S, Qiu J, Zhu C. Photoinduced formation of colloidal Au by a near-infrared femtosecond laser. Journal of Materials Research. 2003;**18**:1710

[18] Nakamura T, Herbani Y, Ursescu D, Banici R, Dabu RV, Sato S. Spectroscopic study of gold nanoparticle formation through high intensity laser irradiation of solution. AIP Advances. 2013;**3**:082101

[19] Tangeysh B, Moore Tibbetts K, Odhner JH, Wayland BB, Levis RJ. Gold nanoparticle synthesis using spatially and temporally shaped femtosecond laser pulses: Post-irradiation auto-reduction of aqueous $[AuCl_4]^-$. Journal of Physical Chemistry C. 2013;**117**:18719

[20] Odhner JH, Moore Tibbetts K, Tangeysh B, Wayland BB, Levis RJ. Mechanism of improved Au nanoparticle size distributions using simultaneous spatial and temporal focusing for femtosecond laser irradiation of aqueous $KAuCl_4$. Journal of Physical Chemistry C. 2014; **118**:23986

[21] Uwada T, Wang S-F, Liu T-H, Masuhara H. Preparation and micropatterning of gold nanoparticles by femtosecond laser-induced optical breakdown. Journal of Photochemistry and Photobiology A. 2017;**346**:177

[22] Herbani Y, Nakamura T, Sato S. Synthesis of platinum-based binary and ternary alloy nanoparticles in an intense laser field. Journal of Colloid and Interface Science. 2012;**375**:78

[23] Sarker MSI, Nakamura T, Herbani Y, Sato S. Fabrication of Rh based solid-solution bimetallic alloy nanoparticles with fully-tunable composition through femtosecond laser irradiation in aqueous solution. Applied Physics A: Materials Science & Processing. 2012; **110**:145

[24] Tangeysh B, Moore Tibbetts K, Odhner JH, Wayland BB, Levis RJ. Triangular gold nanoplate growth by oriented attachment of Au seeds generated by strong field laser reduction. Nano Letters. 2015;**15**:3377

[25] Tangeysh B, Tibbetts KM, Odhner JH, Wayland BB, Levis RJ. Gold nanotriangle formation through strong-field laser processing of aqueous $KAuCl_4$ and postirradiation reduction by hydrogen peroxide. Langmuir. 2017;**33**:243

[26] Belmouaddine H, Shi M, Karsenti P-L, Meesat R, Sanche L, Houde D. Dense ionization and subsequent non-homogeneous radical-mediated chemistry of femtosecond laser-induced low density plasma in aqueous solutions: Synthesis of colloidal gold. Physical Chemistry Chemical Physics. 2017;**19**:7897

[27] Nakashima N, Yamanaka K, Saeki M, Ohba H, Taniguchi S, Yatsuhashi T. Metal ion reductions by femtosecond laser pulses with micro-joule energy and their efficiencies. Journal of Photochemistry and Photobiology A. 2016;**319–320**:70

[28] Rodrigues CJ, Bobb J, John MG, Fisenko S, El-Shal MSl, Tibbetts KM. Photochemical reduction of $[AuCl_4]^-$ with nanosecond and femtosecond laser pulses: Electrons or heat?. 2018. in preparation

[29] Ferreira PHD, Vivas MG, Boni LD, dos Santos DS, Balogh DT, Misoguti L, Mendonca CR. Femtosecond laser induced synthesis of Au nanoparticles mediated by chitosan. Optics Express. 2012;**20**:518

[30] Lu W-E, Zheng M-L, Chen W-Q, Zhao Z-S, Duan X-M. Gold nanoparticles prepared by glycinate ionic liquid assisted multi-photon photoreduction. Physical Chemistry Chemical Physics. 2012;**14**:11930

[31] Keldysh L. Ionization in field of a strong electromagnetic wave. Soviet Physics - JETP. 1965;**20**:1307

[32] Shen YR. The Principles of Nonlinear Optics. New York: Wiley; 1984

[33] Noack J, Vogel A. Laser-induced plasma formation in water at nanosecond to femtosecond time scales: Calculation of thresholds, absorption coefficients, and energy density. IEEE Journal of Quantum Electronics. 1999;**35**:1156

[34] Vogel A, Noack J, Hüttman G, Paltauf G. Mechanisms of femtosecond laser nanosurgery of cells and tissues. Applied Physics B. 2005;**81**:1015

[35] Liu W, Kosareva O, Golubtsov I, Iwasaki A, Becker A, Kandidov V, Chin S. Femtosecond laser pulse filamentation versus optical breakdown in H_2O. Applied Physics B: Lasers and Optics. 2003;**76**:215

[36] Kandidov V, Kosareva O, Golubtsov I, Liu W, Becker A, Akozbek N, Bowden C, Chin S. Self-transformation of a powerful femtosecond laser pulse into a white-light laser pulse in bulk optical media (or supercontinuum generation). Applied Physics B: Lasers and Optics. 2003;**77**:149

[37] Couairon A, Mysyrowicz A. Femtosecond filamentation in transparent media. Physics Reports. 2007;**441**:47

[38] Linz N, Freidank S, Liang X-X, Vogel A. Wavelength dependence of femtosecond laser-induced breakdown in water and implications for laser surgery. Physical Review B. 2016; **94**:024113

[39] Elles CG, Jailaubekov AE, Crowell RA, Bradforth SE. Excitation-energy dependence of the mechanism for two-photon ionization of liquid H_2O and D_2O from 8.3 to 12.4 eV. The Journal of Chemical Physics. 2006;**125**:044515

[40] Linz N, Freidank S, Liang X-X, Vogelmann H, Trickl T, Vogel A. Wavelength dependence of nanosecond infrared laser-induced breakdown in water: Evidence for multiphoton initiation via an intermediate state. Physical Review B. 2015;**91**:134134

[41] Fan CH, Sun J, Longtin JP. Breakdown threshold and localized electron density in water induced by ultrashort laser pulses. Journal of Applied Physics. 2002;**91**:2530

[42] Efimenko ES, Malkov YA, Murzanev AA, Stepanov AN. Femtosecond laser pulse-induced breakdown of a single water microdroplet. Journal of the Optical Society of America B: Optical Physics. 2014;**31**:534

[43] Marburger J. Self-focusing: Theory. Progress in Quantum Electronics. 1975;**4**:35

[44] Brodeur A, Chin SL. Band-gap dependence of the ultrafast white-light continuum. Physical Review Letters. 1998;**80**:4406

[45] Besner S, Kabashin AV, Winnik FM, Meunier M. Synthesis of size-tunable polymer-protected gold nanoparticles by femtosecond laser-based ablation and seed growth. Journal of Physical Chemistry C. 2009;**113**:9526

[46] Besner S, Kabashin AV, Meunier M. Fragmentation of colloidal nanoparticles by femtosecond laser-induced supercontinuum generation. Applied Physics Letters. 2006;**89**: 233122

[47] Besner S, Kabashin A, Meunier M. Two-step femtosecond laser ablation-based method for the synthesis of stable and ultra-pure gold nanoparticles in water. Applied Physics A: Materials Science & Processing. 2007;**88**:269

[48] Minardi S, Gopal A, Tatarakis M, Couairon A, Tamošauskas G, Piskarskas R, Dubietis A, Trapani PD. Time-resolved refractive index and absorption mapping of light-plasma filaments in water. Optics Letters. 2008;**33**:86

[49] Minardi S, Gopal A, Couairon A, Tamoašuskas G, Piskarskas R, Dubietis A, Trapani PD. Accurate retrieval of pulse-splitting dynamics of a femtosecond filament in water by time-resolved shadowgraphy. Optics Letters. 2009;**34**:3020

[50] Besner S, Meunier M. Femtosecond laser synthesis of AuAg nanoalloys: Photoinduced oxidation and ions release. Journal of Physical Chemistry C. 2010;**114**:10403

[51] Chin SL, Lagacé S. Generation of H_2, O_2, and H_2O_2 from water by the use of intense femtosecond laser pulses and the possibility of laser sterilization. Applied Optics. 1996;**35**:907

[52] Kurihara K, Kizling J, Stenius P, Fendler JH. Laser and pulse radiolytically induced colloidal gold formation in water and in water-in-oil microemulsions. Journal of the American Chemical Society. 1983;**105**:2574

[53] Crowell RA, Bartels DM. Multiphoton ionization of liquid water with 3.0–5.0 eV photon. The Journal of Physical Chemistry. 1996;**100**:17940

[54] Reuther A, Laubereau A, Nikogosyan DN. Primary photochemical processes in water. The Journal of Physical Chemistry. 1996;**100**:16794

[55] Pommeret S, Gobert F, Mostafavi M, Lampre I, Mialocq J-C. Femtochemistry of the hydrated electron at decimolar concentration. The Journal of Physical Chemistry. A. 2001;**105**:11400

[56] Nikogosyan DN, Oraevsky AA, Rupasov VI. Two-photon ionization and dissociation of liquid water by powerful laser UV radiation. Chemical Physics. 1983;**77**:131

[57] Behar D, Rabani J. Kinetics of hydrogen production upon reduction of aqueous TiO_2 nanoparticles catalyzed by Pd^0, Pt^0, or Au^0 coatings and an unusual hydrogen abstraction; steady state and pulse radiolysis study. The Journal of Physical Chemistry. B. 2006; **110**:8750

[58] Zayats M, Baron R, Popov I, Willner I. Biocatalytic growth of Au nanoparticles: From mechanistic aspects to biosensors design. Nano Letters. 2005;**5**:21

[59] McGilvray KL, Granger J, Correia M, Banks JT, Scaiano JC. Opportunistic use of tetrachloroaurate photolysis in the generation of reductive species for the production of gold nanostructures. Physical Chemistry Chemical Physics. 2011;**13**:11914

[60] LaMer VK, Dinegar RH. Theory, production and mechanism of formation of monodispersed hydrosols. Journal of the American Chemical Society. 1950;**72**:4847

[61] Yan H, Cingarapu S, Klabunde KJ, Chakrabarti A, Sorensen CM. Nucleation of gold nanoparticle superclusters from solution. Physical Review Letters. 2009;**102**:095501

[62] Turkevich J, Stevenson PC, Hillier J. A Study of the nucleation and growth processes in the synthesis of colloidal gold. Discussions of the Faraday Society. 1951;**11**:55

[63] Takiyama K. Formation and aging of precipitates. VIII. Formation of monodisperse particles (I) Gold sol particles by sodium citrate method. Bulletin of the Chemical Society of Japan. 1958;**31**:944

[64] Esumi K, Hosoya T, Suzuki A, Torigoe K. Spontaneous formation of gold nanoparticles in aqueous solution of sugar-persubstituted poly(amidoamine)dendrimers. Langmuir. 2000; **16**:2978

[65] Shields SP, Richards VN, Buhro WE. Nucleation control of size and dispersity in aggregative nanoparticle growth. A study of the coarsening kinetics of thiolate-capped gold nanocrystals. Chemistry of Materials. 2010;**22**:3212

[66] Njoki PN, Luo J, Kamundi MM, Lim S, Zhong C-J. Aggregative growth in the size-controlled growth of monodispersed gold nanoparticles. Langmuir. 2010;**26**:13622

[67] Watzky MA, Finke RG. Transition metal nanocluster formation kinetic and mechanistic studies. A new mechanism when hydrogen is the reductant: Slow, continuous nucleation and fast autocatalytic surface growth. Journal of the American Chemical Society. 1997;**119**: 10382

[68] Finney EE, Finke RG. Nanocluster nucleation and growth kinetic and mechanistic studies: A review emphasizing transition-metal nanoclusters. Journal of Colloid and Interface Science. 2008;**317**:351

[69] Piella J, Bastús NG, Puntes V. Size-Controlled Synthesis of Sub-10-nanometer Citrate-Stabilized Gold Nanoparticles and Related Optical Properties. Chemistry of Materials. 2016;**28**:1066

[70] Haiss W, Thanh NTK, Aveyard J, Fernig DG. Determination of size and concentration of gold nanoparticles from UV-vis spectra. Analytical Chemistry. 2007;**79**:4215

[71] Oron D, Silberberg Y. Spatiotemporal coherent control using shaped, temporally focused pulses. Optics Express. 2005;**13**:9903

[72] Faccio D, Tamošauskas G, Rubino E, Darginavičius J, Papazoglou DG, Tzortzakis S, Couairon A, Dubietis A. Cavitation dynamics and directional microbubble ejection induced by intense femtosecond laser pulses in liquids. Physical Review E. 2012;**86**:036304

[73] Meader VK, John MG, Frias Batista LM, Ahsan S, Tibbetts KM. Radical chemistry in a femtosecond laser plasma: Photochemical reduction of Ag^{+} in liquid ammonia solution. Molecules. 2018;**23**:532

[74] LaVerne JA, Pimblott SM. Scavenger and time dependences of radicals and molecular products in the electron radiolysis of water: Examination of experiments and models. The Journal of Physical Chemistry. 1991;**95**:3196

[75] Herbani Y, Nakamura T, Sato S. Silver nanoparticle formation by femtosecond laser induced reduction of ammonia-containing $AgNO_3$ solution. Journal of Physics Conference Series. 2017;**817**:012048

[76] Goia D, Matijevi'c E. Tailoring the particle size of monodispersed colloidal gold. Colloids and Surfaces, A: Physicochemical and Engineering Aspects. 1999;**146**:139

[77] Wang S, Qian K, Bi X, Huang W. Influence of speciation of aqueous $HAuCl_4$ on the synthesis, structure, and property of Au colloids. Journal of Physical Chemistry C. 2009; **113**:6505

[78] Ni W, Kou X, Yang Z, Wang J. Tailoring longitudinal surface plasmon wavelengths, scattering and absorption cross sections of gold nanorods. ACS Nano. 2008;**2**:677

[79] Oh E, Susumu K, Goswami R, Mattoussi H. One-phase synthesis of water-soluble gold nanoparticles with control over size and surface functionalities. Langmuir. 2010;**26**:7604

IntechOpen